ACS SENSORS

pubs.acs.org/acssensors

Article

Ultrathin, Biocompatible, and Flexible Pressure Sensor with a Wide Pressure Range and Its Biomedical Application

Yongrok Jeong, Jaeho Park, Jinwoo Lee, Kyuyoung Kim, and Inkyu Park*

Cite This: *ACS Sens.* 2020, 5, 481−489

Read Online

ACCESS | Metrics & More | Article Recommendations | Supporting Information

ABSTRACT: In this research, an ultrathin, biocompatible, and flexible pressure sensor with a wide pressure range has been developed and applied in biomedical applications. The pressure sensing mechanism is based on the variation of contact resistance between an electrode and a three-dimensional microstructured polyimide/carbon nanotube composite film. The sensor has a thickness of about 31.3 μm, a maximum sensitivity of 41.0 MPa^{-1}, and a sensing range of 10−500 kPa. Moreover, in situ temperature measurement by an integrated resistive temperature detector enables data correction for varying temperature conditions. In order to show the advantages of the fabricated sensor, it is attached to the human body and integrated with the surface of a radiofrequency ablation (RFA) needle with small radius of curvature. In the experiments, the proposed pressure sensor measured subtle pressure levels (pulse pressure) and high pressure levels (fingertip pressure) without losing conformal contact with the skin. In addition, when the pressure-sensor-integrated RFA needle was inserted into a bovine liver, successful detection of steam popping phenomenon was observed.

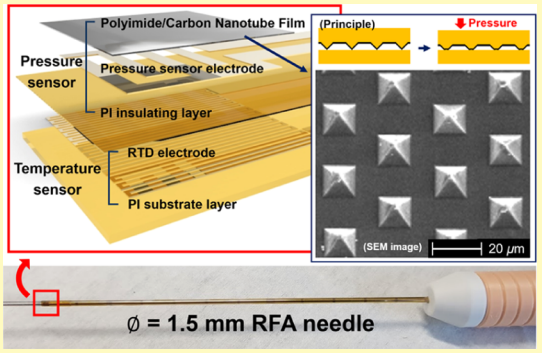

KEYWORDS: *flexible pressure sensor, biomedical sensor, ultrathin sensor, carbon nanotube, radiofrequency ablation*

Recently, flexible pressure sensors are being actively studied owing to their potential for a wide range of applications, such as electronic skins,[1,2] electronic textiles,[3] flexible touch displays,[4] soft robotics,[5] mobile health care aids,[6] and energy harvesting.[7] In general, composite materials made by mixing flexible polymers and conductive nanomaterials in a matrix with an active filler have been frequently used to fabricate flexible pressure sensors. Among the polymers, elastomeric materials with high stretchability, such as polydimethylsiloxane (PDMS) and Ecoflex, have been frequently utilized as substrates for flexible pressure sensors.[4,6,8−15] However, they have low elastic moduli of 10 kPa to 10 MPa; thus, the deformation limits of these sensors are relatively low, and the sensor signals saturate at low pressure levels. Moreover, although the stretchabilities of polymers such as PDMS and Ecoflex are one of their major advantages, they may cause adverse effects (e.g., warpage, wrinkling, or tearing) to ultrathin sensor structures during fabrication or assembly. To achieve ultrathin devices, the matrix polymer should be adequately stiff. In this regard, we have reviewed previous studies on thin flexible pressure sensors covering a wide pressure range. One research suggested a pressure sensor using laser-scribed graphene (LSG) as a functional layer.[16] The pressure was measured using the change in contact resistance between two LSG layers, whose thickness was only 40 μm, but pressure measurements of only up to 50 kPa could be achieved. Another research suggested a capacitive pressure sensor using micropatterned pyramidal ionic gels as a functional layer and indium tin oxide as an electrode.[17] Although the thickness of the functional layer was 15 μm, this sensor could only cover a small pressure range of up to 50 kPa. Another study suggested a resistive pressure sensor using a gel formed by polypyrrole (PPy) bubbles as the functional layer.[18] In this work, micropatterns of the gel made of hollow PPy spheres were used to measure the pressure; the sensor had a thickness of 181 μm and a sensing range of up to 100 kPa.

Although the thickness of the sensor can be significantly reduced using various materials from previous research, the pressure sensing range has not been broadened sufficiently. To solve this problem, we adopted polyimide (PI), with sufficiently high elastic modulus compared to other polymers, as the matrix polymer. However, the high stiffness of PI does not allow large deformation by applied pressure, thus rendering low sensitivity of the pressure sensor. Therefore, surface microstructuring of the PI film was employed to enhance the sensitivity of the pressure sensor. This method can be found in many previous research studies.[11,18,19] Although the methods provided in these studies used micropyramidal patterns, only soft materials such as PDMS and PPy gel were used. Therefore,

Received: November 15, 2019
Accepted: February 5, 2020
Published: February 5, 2020

we have adopted the microstructuring of the PI with high elastic modulus as an advantage to cover a broad pressure range.

In this research, we developed a novel flexible pressure sensor with an ultrasmall thickness (31.3 μm) and a wide pressure sensing range (10−500 kPa). This sensor is based on the principle of change of contact resistance between a three-dimensional microstructured conductive film and a sensor electrode due to the applied pressure. To enlarge the dynamic range of the pressure sensor, we employed PI with a high elastic modulus (2.55 GPa) and carbon nanotubes (CNTs) as the matrix and filler material, respectively. The surface of the conductive film was microstructured in a pyramidal shape, and the contact area between the conductive film and the electrode increased as the applied pressure was increased. For more accurate sensing, the possibility of temperature compensation was also suggested.

One of the most important advantages of the thin sensor is bendability. If the sensor is thin, it can be attached to curved surfaces with smaller radii of curvature more easily because of reduced bending stresses. In order to prove this advantage, applications such as direct attachment of the sensor to the human body with conformal contact for wrist pulse or tactile pressure measurement and direct integration with a radio-frequency ablation (RFA) needle having radius of curvature 0.75 mm for tissue pressure measurement were demonstrated.

In the case of the former application, the fabricated sensor was affixed to the human body to measure the pressure. First, the sensor was applied to the wrist and neck, and it was used to measure the pulse pressure. Second, the sensor was attached to the fingertip and used to measure the interaction between the fingertip and the external environment.

In the case of second application, the fabricated sensor was integrated with the surface of a RFA needle of diameter 1.5 mm to monitor the pressure changes associated with the "steam popping" phenomenon during the RFA procedure. For this application, the sensor should be attached on a surface with a small radius of curvature (0.75 mm) and should be capable of measuring a wide pressure range (pressure difference exceeding 125 kPa[20]).

SENSING MECHANISM AND FABRICATION

Sensing Mechanism. The proposed sensor consists of a pressure sensor and a temperature sensor, formed in a multilayer structure, as shown in Figure 1a.

The pressure sensor operates on the basis of change in contact resistance between the microstructured polyimide/carbon nanotube (PI/CNT) film and the electrode according to the applied pressure. The shape of the microstructure was chosen as pyramidal in order to maximize the sensitivity of the sensor. Owing to the stress concentration at the pointed end (tip of the micropyramid), the maximal contact area change of the microstructured PI/CNT film can be achieved. The scanning electron microscopy image (top view) of the fabricated PI/CNT film is shown in Figure 1b. Here, the micropyramids are ordered in hexagonal pattern and are formed uniformly. A cross-sectional image of the fabricated micropyramids is shown in Figure 1c. The thickness of the PI/CNT film is measured as approximately 8 μm without the pyramids and 15 μm with the pyramids. Figure 1c(ii) shows the magnified view of the PI/CNT film. Here, we can observe the net-shaped CNT film on the surface and the penetrating PI between the CNTs, which may hold the CNTs together

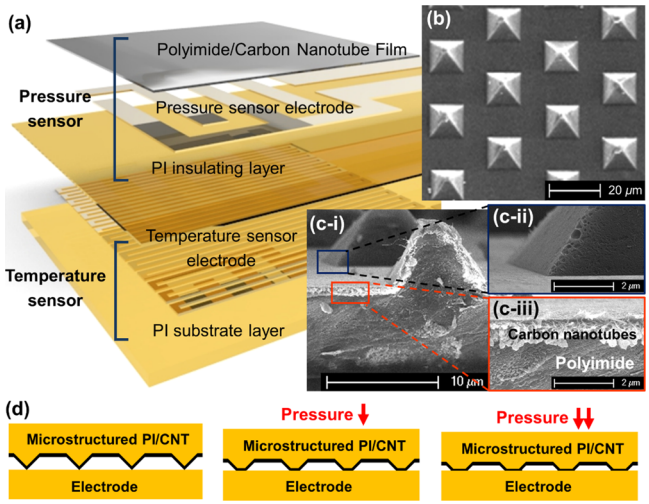

Figure 1. Overview of the PI-/CNT-based pressure sensor: (a) schematic of the proposed sensor device composed of an RTD temperature sensor and a pressure sensor based on 3D microstructured PI/CNT composite; (b) top view of the fabricated microstructures of PI/CNT composite from top side; (c) cross-sectional view of the fabricated microstructures of PI/CNT composite (i), magnified image of the wall side of the micropyramid (ii), magnified image of the cross section of the PI/CNT film (iii); and (d) concept drawing of the deformation tendency of the PI/CNT film with increasing pressure.

tightly. Figure 1c(iii) shows the magnified view of the boundary between the CNT and the PI. The CNT layer has a thickness of about 1 μm, and the CNTs are tangled in a single layer. In addition, the CNTs are exposed on the bare surface. From these results, it can be concluded that the conductivity of the PI/CNT film was appropriately formed and enabled by the CNT layer.

Figure 1d conceptualizes the morphological changes in the micropyramidal PI/CNT film. This change in the contact area between the PI/CNT film and the electrode causes conductance changes with an applied pressure.

The temperature sensor uses the principle of a resistance temperature detector (RTD) and monitors the temperature in the environment to compensate for the temperature effect on the pressure sensor.

Fabrication. *Fabrication Method.* The entire fabrication step can be divided into three parts: fabrication of the electrode, fabrication of the PI/CNT functional film, and assembly of the sensor. First, the electrode was fabricated in several steps by spin coating the PI film, lift-off by lithography, and E-beam metal deposition method (Figure 2a). The first layer was the RTD electrode, and the second layer comprised the pressure sensor electrode. Next, the PI/CNT functional film was fabricated. Microstructuring through the conventional tetramethylammonium hydroxide etching method of the (100) oriented silicon wafer was adopted to fabricate the silicon mold for the PI/CNT film, and the PI/CNT film was fabricated via subsequent CNT spray coating and PI spin coating (Figure 2b). Finally, the micropatterned PI/CNT film was detached using PI tape and transferred to the electrode with fixation via the PI tape, which used in the detachment step.

Fabrication Results. An optical microscopy image of the fabricated sensor is shown in Figure 2e. Here, the thick and bright lines are the electrodes of the pressure sensor, whereas the thin and bright lines are the electrodes of the RTD sensor.

https://dx.doi.org/10.1021/acssensors.9b02260
ACS Sens. 2020, 5, 481−489

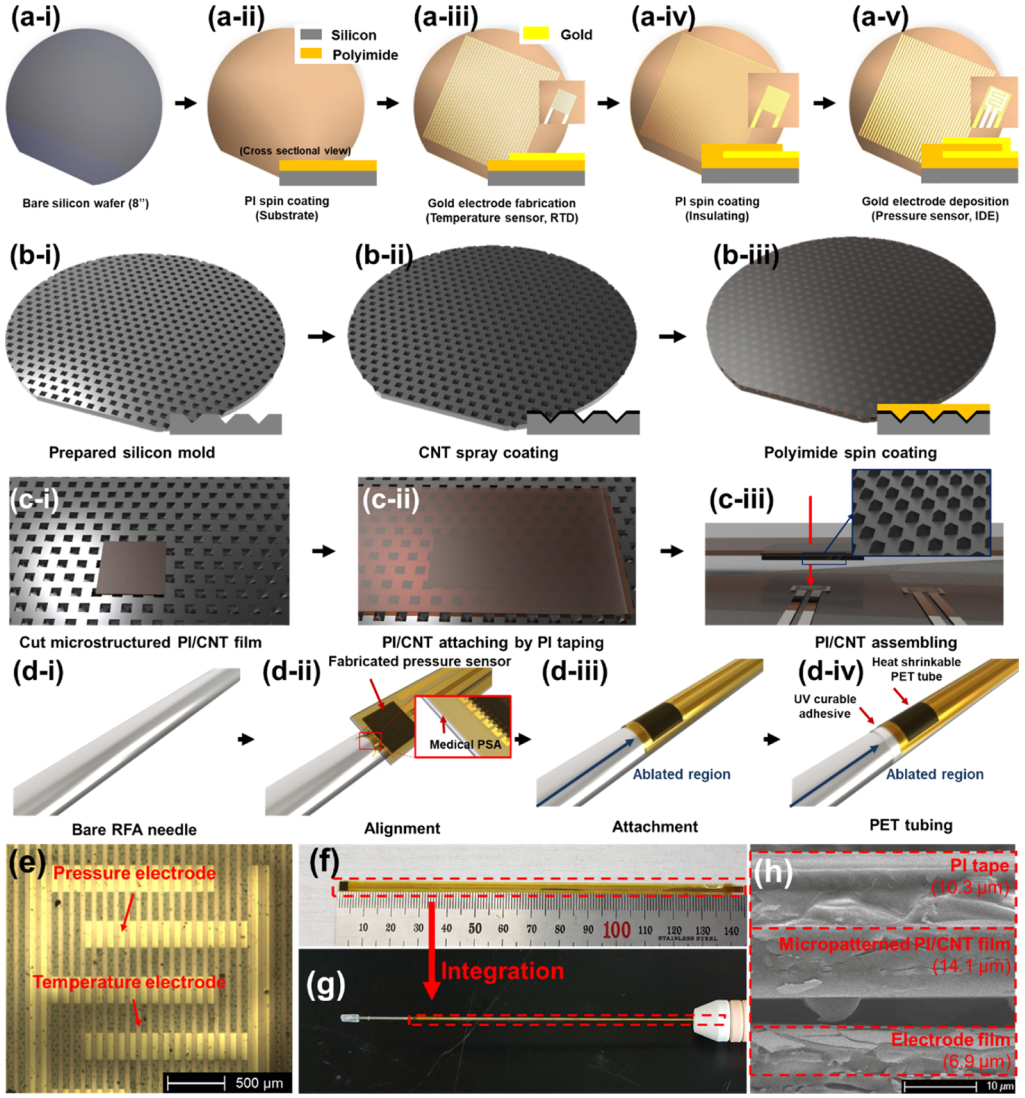

Figure 2. Schematic flow diagrams and results of the fabrication: (a) fabrication of the electrode layer; (b) fabrication of the PI/CNT film using fabricated micropyramid mold; (c) assembly of the pressure sensor; (d) attachment of the pressure sensor on the bare RFA needle; (e) micrograph of the fabricated PI-/CNT-based pressure sensor; (f–g) whole view of the fabricated pressure sensor strip and integration result on the RFA needle; and (h) cross-sectional view of the fabricated pressure sensor.

In addition, the fabricated sensor has a length of 145 mm and thickness of 31.3 μm (Figure 2f–h).

In order to fabricate the PI/CNT film, the CNTs are first deposited on the surface of the silicon mold and coated with PI (Figure 2b). The CNT side (bottom) of the coated PI/CNT film contacts the wafer surface directly, thereby following the three-dimensional geometry of the silicon mold; this allows the microstructuring of the PI/CNT film.

RESULTS AND DISCUSSION

Sensor Characterization. *Background for Sensor Characterization.* Theoretically, it is well known that the relationship between the contact resistance and applied force is deduced from the following equation[21]

$$R_c = \left(\frac{\rho^2 \eta \pi U}{4F}\right)^{1/2} \quad (1)$$

where ρ is the electrical resistivity, η is an empirical coefficient, H is the hardness of the material, and F is the load. From this relationship, and with the assumption of no significant change in the environment of the experimental setup, a linear relationship can be concluded between log R_c and log F.

The resistance of the proposed PI/CNT-based pressure sensor can be written as follows

$$R_t = R_f + R_c \quad (2)$$

where R_t is the total resistance, R_f is the film resistance, and R_c is the contact resistance. Because of the low electromechanical change in the conductive film of the sensor with high elastic modulus, there is no significant change in R_f. Therefore, the change in total resistance is dominated by that of R_c. As mentioned previously, eq 1 demonstrates a linear relationship between log F and log R_c. Here, log F can be converted to a linear function of log P, where P is the applied pressure. Further, log R_c can be converted to a linear function of log G_c, where G_c is the contact conductance. Thus, a linear relationship between log P and log G_c can be concluded. Through this relationship, sensor characteristics such as

https://dx.doi.org/10.1021/acssensors.9b02260
ACS Sens. 2020, 5, 481−489

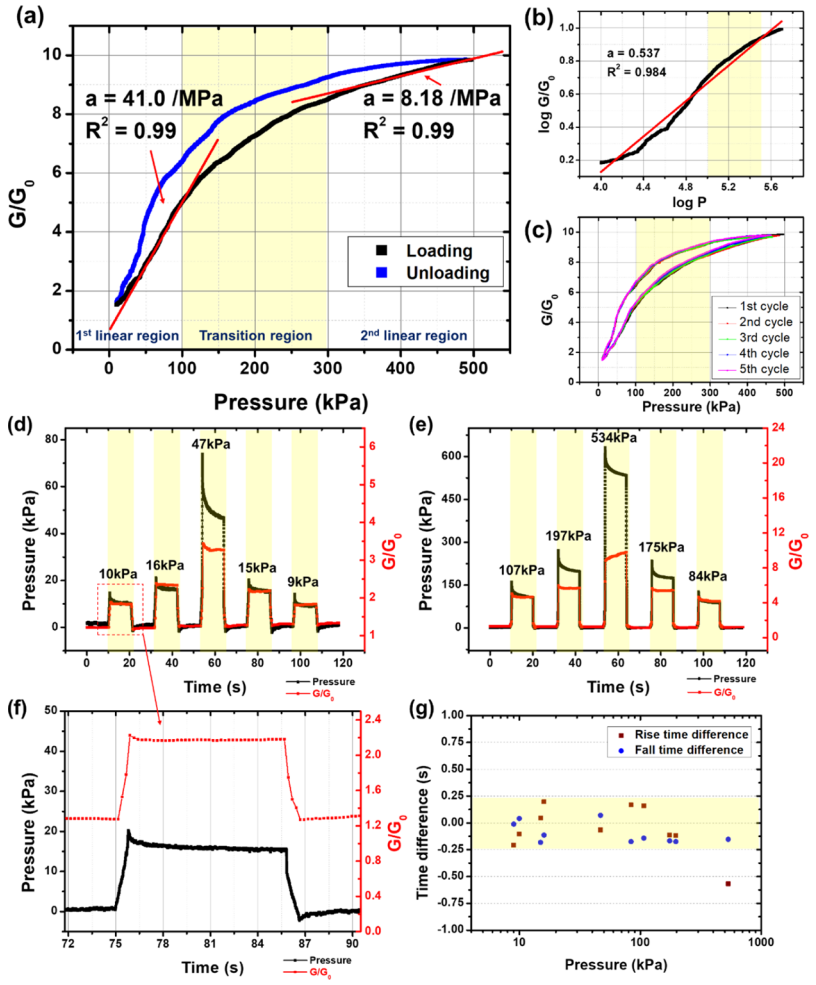

Figure 3. Characterization result of the fabricated pressure sensor: (a) static pressure response of the PI-/CNT-based pressure sensor; (b) log–log plot of the sensor response vs static pressure of the PI-/CNT-based pressure sensor during pressure loading. The region indicated with an yellow box is the transition region and (c) sensor response for five consecutive loading–unloading cycles for the repeatability test. The region indicated with an yellow box is the transition region and (d) dynamic pressure response test results for 10, 20, and 50 kPa. The written pressure value indicates the actual pressure and (e) dynamic pressure response test results for 100, 200, and 500 kPa. The written pressure value indicates the actual pressure; (f) magnified plot of the dynamic test for P = 10 kPa; and (g) calculated results for the rise and fall time differences between the reference load cell and 3D microstructured PI-/CNT composite-based sensor.

sensitivity were also analyzed using a log–log plot of the static pressure response curve.

Sensor Characterization. The sensor response was analyzed using normalized conductance (G/G_0), where G and G_0 are the conductance of the sensor with and without applied pressure, respectively. The sensitivity is defined as $(\Delta(G/G_0)/\Delta P)$, where P is the pressure.

Figure 3a shows the static pressure response curve of the PI/CNT-based sensor on a linear scale. As shown, the sensing range can be divided into three distinct regions: two linear regions and a nonlinear transition region. The first region shows a linear relationship between G/G_0 and P, with a sensitivity of 41.0 MPa^{-1} and an R^2 value of 0.99. The sensitive variation of the signal originated from the sharp tip of the structure and newly formed contact. In the sensor assembly step, it is difficult to achieve conformal contact between the PI/CNT film and the electrode. This causes a decrease in the initial conductance. The second region shows a nonlinear transition between the first and second linear regions. Finally, the third region again shows a linear relationship between G/G_0 and P, with a sensitivity of 8.18 MPa^{-1} and an R^2 value of 0.99. The sensor shows a stable response in the pressure range of 10–500 kPa.

In Figure 3a, the difference between the loading and unloading curves was also observed as a result of hysteresis. This hysteretic behavior may be caused by three reasons: first, it may be due to the viscoelastic behavior of the PI.[22−24] Because of the large elastic modulus of the PI, there may be no significant hysteretic effect in the case of small deformation. However, owing to the sharp structure of the micropyramidal tip end, high stress is concentrated at the tip end. This may cause a sufficiently large deformation at the tip end to reveal the viscoelastic behavior. Second, a pressure-sensitive adhesive (PSA) was utilized to attach the PI/CNT film and the electrode. As the main ingredient of the adhesive is silicone, the hysteretic behavior may originate from it. Third, the adhesion energy between the electrode and the PI/CNT film can cause hysteresis. During the loading cycle, the contact was newly made, which may not be affected by the adhesion energy. However, during the unloading cycle, the contact was already formed, so the detachment of the PI/CNT film may be

https://dx.doi.org/10.1021/acssensors.9b02260
ACS Sens. 2020, 5, 481−489

possibly harder than attachment owing to the additional adhesion energy.

According to eq 1, a linear relationship between log P and log G was deduced, and this linear relationship was applied equivalently to the relationship between log P and log G/G_0. This linear relationship can be verified by the log−log plot for the experimental data of the static pressure sensing test shown in Figure 3b. From this plot, we observe a linear relationship with a slope of 0.537 and an R^2 of 0.984. This verifies that the theoretical model with a linear relationship between log G and log P with a coefficient of 0.5 matches well with the experimental result of our sensor.

For the same sensor, five loading−unloading cyclic tests were performed. As shown in Figure 3c, no significant change was observed in the sensor signal during the five loading cycles. From this experiment, we can conclude that the sensor does not experience undesirable plastic deformation in the pressure range of 10−500 kPa. In addition, the stability test for 1000 cycles of loading−unloading between 7 and 570 kPa reveals that the sensor is capable of stable and repeatable operation for many loading cycles (Figure S1).

Figure 3d−g shows the dynamic pressure responses of the fabricated pressure sensor. In this experiment, the real-time responses of the sensor to P = 10, 20, 50, 100, 200, and 500 kPa were measured, as presented in Figure 3d,e. The sensor shows stable and quick responses to both low-pressure values (Figure 3d) and high-pressure values (Figure 3e). Here, the proposed sensor shows an overshoot of the signal when the pressure is applied. Possible reasons for this transient response with overshoot followed by slow saturation may be due to not only the inherent dynamic characteristics of the actuator used in the compression test but also the viscoelastic property of the polymer (i.e., PI) in our sensor.

Owing to the limitation of the actuator's dynamics, a perfect step-motion input is not possible, and thus, it is difficult to evaluate the dynamic characteristics of the sensor from its transient response. Instead, we compared the transient response of our sensor to that of the reference load cell. In this comparison, the rise time from 10 to 90% (T_{10-90}) and the fall time from 90 to 10% (T_{90-10}) were utilized (Figure S2). As shown in Figure 3g, the differences in rise and fall times between the reference load cell and our sensor are in the range of ±0.25 s, which is the possible error range of the used measurement setup. From this set of experiments, it can be concluded that the dynamic characteristics of our sensor are almost identical to those of a commercial load cell, and therefore, our sensor can be useful for real-time pressure detection in a wide range.

Temperature Compensation. In general, the conductance of CNTs is known to increase at higher temperatures owing to their electron hopping nature. In order to consider this factor, the Arrhenius relationship has been adopted as follows.[24−27]

$$G(T) = G_0 e^{-E_a/RT} = G(T_0)e^{-T_0/T} \quad (3)$$

According to the Arrhenius relationship (eq 3), the linear relationship between log $G(T)$ and T^{-1} can be obtained. This relationship can be represented as follows

$$\log G(T) = \log G(T_0) - T_0 T^{-1} \quad (4)$$

where G is the conductance, T is the actual temperature, and T_0 is the reference temperature. In addition, from eq 1, the linear relationship between log $G(T_0)$ and log P can be represented as follows

$$\log P = a + b \log G(T_0) \quad (5)$$

where P is the applied pressure and a, b are the calibration constants. By combining eqs 4 and 5, the relationship between P and $G(T)$ can be concluded as follows

$$\log P = a + b \log G(T) + c\ T^{-1} \quad (6)$$

where c is the calibration constant. As this equation is only composed of the present values of pressure, conductance, and temperature, we can calculate the values of a, b, and c from the experimental results. Through the obtained b and c values, we can first calculate $G(T_0)$ from $G(T)$ and T. In the analysis, $G(T_0)$ was used instead of $G(T)$ because it represents the temperature-compensated conductance value through the Arrhenius relationship.

For the temperature compensation test, the relationship between temperature and conductance of the pressure sensor was analyzed for varying temperatures between T = 23.5 °C and T = 100 °C (Figure S3). Here, T = 23.5 °C was chosen to simulate the room temperature, and T = 100 °C was chosen to simulate the water boiling temperature, which is the maximum possible temperature during the steam popping phenomenon.

The temperature test results show that the conductance of the fabricated sensor has a positive temperature coefficient, as shown in Figure 4b. From these measurements, the calibration

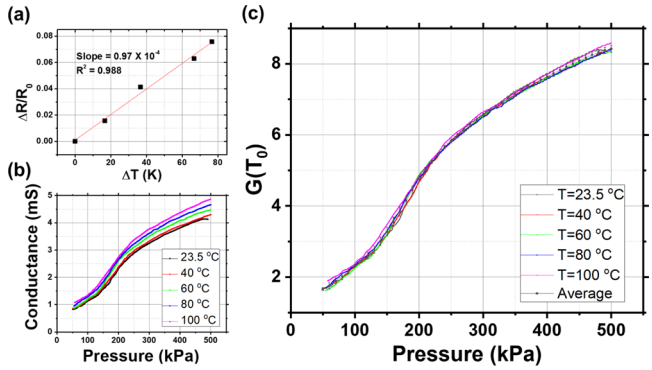

Figure 4. Temperature compensation result: (a) calibration result of the RTD sensor; (b) relationship between conductance and pressure for different temperatures. Because the conductance of the CNT varies depending on the temperature, the G−P curves are different depending on the temperature and (c) temperature compensation result of the PI-/CNT-based pressure sensor through the Arrhenius relationship. $G(T_0)$ values were averaged and the standard deviation was calculated for the pressure in steps of 10 kPa.

constants can be obtained (a = 10.28 Pa, b = 1.276 Pa/mS, and c = 268 Pa·K). Using these parameters, the relationship between $G(T_0)$ and P can be obtained as shown in Figure 4c. Here, each curve indicates loading data at a different temperature, and it is clearly observed that the relationships between the temperature-compensated conductance $G(T_0)$ and pressure P are independent of the temperature.

Application. *Conformal Contact with Human Body.* One of the major applications of the flexible pressure sensor is the measurement of signal from the human body. The measurement of body signals has difficulties for low signal levels and for maintaining contact between the sensor and body. Owing to this nature, the measurement of the body signal is impeded

https://dx.doi.org/10.1021/acssensors.9b02260
ACS Sens. 2020, 5, 481−489

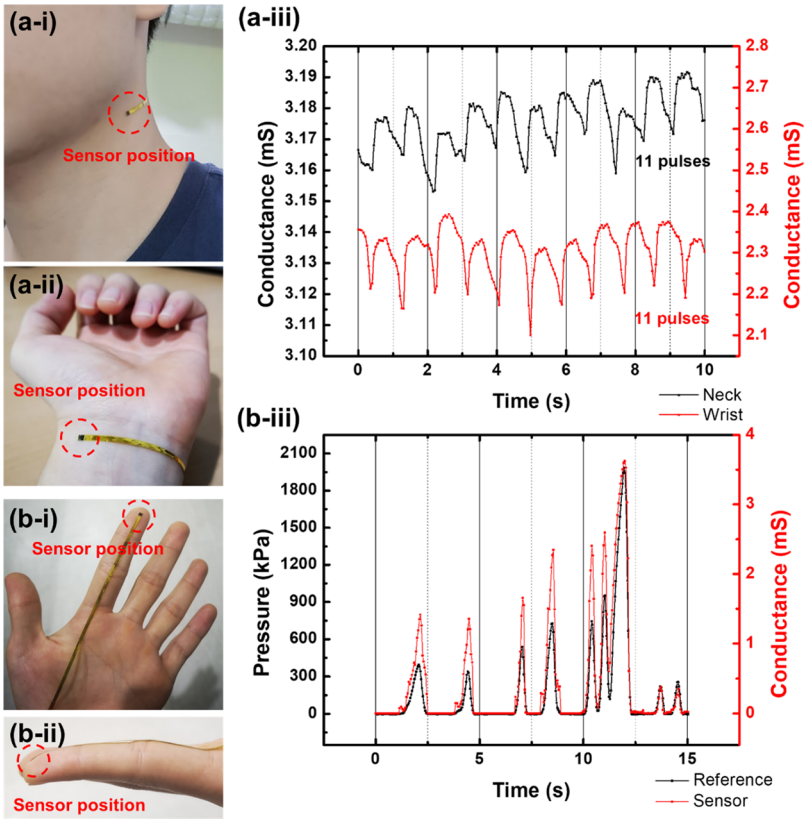

Figure 5. Application of the PI-/CNT-based pressure sensor conformally contacted with the human body: (a) measured pulse pressure on neck (i) and wrist (ii). Same heart rates were concluded for both experiments (iii); (b) measured fingertip pressure with pressing the reference pressure sensor. Conformal contact between the finger and the pressure sensor (i,ii) helped to detect the exact amount of pressure (iii).

significantly by environmental factors. However, in the case of this sensor, the thickness is very low (31.3 μm); this helps the sensor to be attached stably on the skin surface even for varying radii of curvature. To verify this advantage, the fabricated sensor was used to detect the pulse pressure and interactions with external environment and the human body.

The first experiment involved measurement of the pulse pressure. The fabricated sensor was attached on the neck (Figure 5a(i)) and the wrist (Figure 5a(ii)), and the change in pressure was measured (Figure 5a(iii)). Here, the same heart rate (~66 bpm) was detected from both neck and wrist. Through this experiment, it is concluded that our sensor contacted with human skin conformally. In addition, with this sensor, it was shown that our sensor could measure pressure in the ultralow regime.

The second experiment involved measurement of the fingertip pressure for pushing action (Figure S4c). Before the experiment, the conformal contact of the sensor on the fingertip was checked (Figure 5b(i,ii)). Through the measurement, the pressure from the reference sensor and conductance from our sensor were shown to have the same tendency, and the reaction of the sensor was fast enough to monitor the external environment. Our sensor can thus detect a wide range of pressure changes without any interference to human motion.

Attachment on a Medical Device. RFA is a promising method to treat a cancer owing to two main advantages: minimal invasiveness and no need of general anesthesia. These advantages reduce the burden of the surgery and help the patients recover more quickly. It has been reported that most patients treated with RFA are required to stay in the hospital for only 2−3 days.[28] In addition, the safety of the RFA procedure has been proved in previous studies as shown by the high survival rate.[29−31] However, owing to a phenomenon called steam popping, which can occur in up to 64.7% of RFA procedures, the safety of RFA is not completely guaranteed.[32] Specifically, steam popping is an explosion that occurs in a weakly bonded tissue boundary when RFA is performed. During RFA, high heat is generated around the affected tissue (the ablated region). The volume of the internal fluid expands as it vaporizes by the generated heat; this volume expansion ultimately causes explosion of the weakly bonded tissue.[33]

Currently, there are no other methods to detect steam popping, except for hearing the explosive sound generated by the steam popping.[34] Because the sound signals can be easily affected by environmental factors and can be absorbed by adjacent tissues, it is hard to clearly detect steam popping through sound measurements alone. To address this problem, in this study, the proposed PI/CNT-based pressure sensor was attached to an RFA needle with a diameter of 1.5 mm for the detection of pressure change occurring by steam popping.

Because the target application of the proposed sensor is the detection of steam popping, biocompatibility needs to be guaranteed. As explained in the Supporting Information, the proposed sensor consists entirely of the materials reported to be biocompatible. Titanium and gold are well-known biocompatible materials used in the electrode of the implantable device. MD-7 is a commercialized biocompatible PSA. Further, many studies have reported that polymer−CNT composites can be used as biocompatible components.[35−40] Furthermore, the fabricated sensor is encapsulated by

https://dx.doi.org/10.1021/acssensors.9b02260
ACS Sens. 2020, 5, 481−489

biocompatible and heat shrinkable polyester tubes, and therefore, the biocompatibility of our needle-integrated sensor is assured.

The RFA needle integrated with our pressure sensor is shown in Figure 2g. In order to filter out noise due to the radiofrequency wave applied to the RFA needle, a passive low-pass filter (LPF) was fabricated and attached to the needle. The radiofrequency used in the RFA process is 400 kHz, and the proposed LPF has a cutoff frequency of 1 kHz, which is enough to reduce the noise from the RFA needle (Figure 6a(ii)). A bovine liver was chosen as the phantom for the

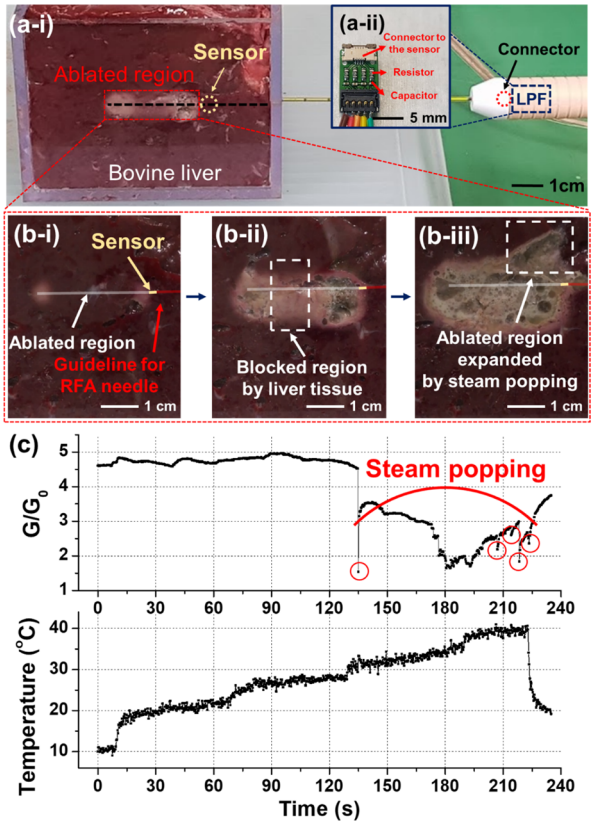

Figure 6. Application of the PI-/CNT-based pressure sensor and attachment on the medical device: (a) experimental setup to monitor the steam popping (i) and the LPF inside the needle casing (ii) for the RFA needle; (b) detailed view of the ablated region in chronological order (i–iii); and (c) example graph showing the detection of steam popping phenomenon. These data were the result of the third experiment in Table 1. (Top) Graph of the normalized conductance change during steam popping events. (Bottom) Graph of temperature change measured by the fabricated RTD during steam popping.

human liver because of its similar electrical properties.[41] This bovine liver was placed in an acryl chamber, as shown in Figure 6a(i). Because the needle is inserted into the human body from the side in the actual RFA procedure, the needle was inserted into the bovine liver through a hole on the sidewall of the acrylic chamber to mimic the real situation.

The detailed ablation process is shown in Figure 6b. During this process, ablation started at both the front and rear edges of the electrically opened area of the RFA needle (Figure 6b(i)); then, the ablated regions expanded (Figure 6b(ii)), and finally, the edges met and formed a wide oval-shaped space (Figure 6b(iii)). In the third step, the part in the ablated region expanded by steam popping is highlighted. An example of the real-time pressure measurement data during the RFA procedure is presented in Figure 6c. A sharp decrease in the sensor signal (normalized conductance) in the graph indicates the steam popping behavior (Movie S1). During the experiment, it was confirmed that steam popping occurred at these points based on sound measurements.

The detectability of the pressure sensor integrated on the RFA needle was evaluated by the ratio of the number of steam poppings detected by the pressure sensor to that by the conventional sound measurement technique. Currently, there exists no standard method to perfectly detect steam popping. Instead, detection of the steam popping through explosive sound measurement was chosen as a reference. Three RFA experiments were performed in total. The fabricated pressure sensor integrated with the RFA needle showed an average detectability of 83.3% (Table 1). The reason why the

Table 1. Experimental Results for the Detection of Steam Popping: Three Experiments Were Performed to Compare the Number of Steam Popping Sounds Detected by a Conventional Sound Measurement Method and by Pressure Measurement with the Pressure Sensor Integrated with the RFA Needle

experiment number	number of steam popping sounds detected	number of steam popping sounds detected by pressure sensor	detectability [%]
1	6	4	66.7
2	1	1	100
3 (Figure 6c)	5	5	100

detectability through the integrated pressure sensor is lower than 100% is thought to be the position of the pressure sensor on the needle. The pressure sensor is located outside the rear edge of the electrically opened area of the RFA needle, as shown in Figure S5. Therefore, if the steam popping occurs on the front edge of the needle, it is possible that the pressure change can be blocked by the liver tissue placed in the middle of the ablated region, and the pressure sensor attached on the rear edge of the needle is not able to detect it.

CONCLUSIONS

In this study, an ultrathin, biocompatible, and flexible pressure sensor based on a microstructured PI/CNT composite film with a wide pressure sensing range was developed, and its feasibility for pressure detection in the RFA procedure was demonstrated. The high elastic modulus of PI allowed the fabrication of the ultrathin pressure sensor with a wide pressure sensing range. The PI/CNT-based pressure sensor showed a maximum sensitivity of 41.0 MPa^{-1} and good stability in the pressure range of 10–500 kPa. In addition, the possibility of temperature compensation of the static pressure response through the integrated RTD sensor was carried out. With its ultrathin property (31.3 μm), our sensor was attached on the neck, wrist, and fingertip to show the advantage of the low thickness and its sensitive response. Moreover, it was attached to the RFA needle of diameter 1.5 mm and used to monitor the internal tissue pressure during RFA procedure and could detect steam popping phenomena with a detectability of 83.3%.

The proposed pressure sensor has unique advantages such as very low thickness, wide pressure sensing range, and

https://dx.doi.org/10.1021/acssensors.9b02260
ACS Sens. 2020, 5, 481–489

biocompatibility compared with other flexible pressure sensors reported to date. Further, the proposed sensor has a thin but rigid property, so it is expected that our sensor can be used in numerous applications. For example, many robotic and industrial manufacturing systems may require pressure sensors with a wide pressure sensing range. This sensor can be one of the solutions with minimal morphological changes to the contact region. In addition, it can be used not only for mechanical systems but also for health monitoring. Last, our sensor may be useful for various biomedical applications such as pressure monitoring on catheters, biopsy needles, stents, and inner brain pressure monitoring because it is ultrathin and biocompatible.

■ ASSOCIATED CONTENT

Supporting Information

The Supporting Information is available free of charge at https://pubs.acs.org/doi/10.1021/acssensors.9b02260.

Detailed fabrication method; detailed experimental method; stability test result; definitions of the rise and fall times; calibration result; experimental setup; and detailed view of the integrated RFA needle (PDF)

Occurrence of steam popping and its detection (MP4)

■ AUTHOR INFORMATION

Corresponding Author

Inkyu Park − *Department of Mechanical Engineering, Korea Advanced Institute of Science and Technology, Daejeon 34141, Republic of Korea;* orcid.org/0000-0001-5761-7739; Email: inkyu@kaist.ac.kr

Authors

Yongrok Jeong − *Department of Mechanical Engineering, Korea Advanced Institute of Science and Technology, Daejeon 34141, Republic of Korea*

Jaeho Park − *Department of Mechanical Engineering, Korea Advanced Institute of Science and Technology, Daejeon 34141, Republic of Korea*

Jinwoo Lee − *RF Medical. Co. Ltd., Seoul 08511, Republic of Korea*

Kyuyoung Kim − *Department of Mechanical Engineering, Korea Advanced Institute of Science and Technology, Daejeon 34141, Republic of Korea*

Complete contact information is available at: https://pubs.acs.org/10.1021/acssensors.9b02260

Author Contributions

The manuscript was written through contributions from all authors. All authors have given approval to the final version of the manuscript.

Notes

The authors declare no competing financial interest.

■ ACKNOWLEDGMENTS

This work was supported by Nano-Convergence Foundation (www.nanotech2020.org) funded by the Ministry of Science, ICT and Future Planning (MSIP, Korea) and the Ministry of Trade, Industry and Energy (MOTIE, Korea) (project number: R201603110). This work was also supported by the National Research Foundation of Korea (NRF) grant funded by the Korea government (MSIT) (no. 2018R1A2B2004910).

■ REFERENCES

(1) Wang, C.; Hwang, D.; Yu, Z.; Takei, K.; Park, J.; Chen, T.; Ma, B.; Javey, A. User-Interactive Electronic Skin for Instantaneous Pressure Visualization. *Nat. Mater.* **2013**, *12*, 899−904.

(2) Jeong, J.-W.; Yeo, W.-H.; Akhtar, A.; Norton, J. J. S.; Kwack, Y.-J.; Li, S.; Jung, S.-Y.; Su, Y.; Lee, W.; Xia, J.; et al. Materials and Optimized Designs for Human-Machine Interfaces via Epidermal Electronics. *Adv. Mater.* **2013**, *25*, 6839−6846.

(3) Lee, J.; Kwon, H.; Seo, J.; Shin, S.; Koo, J. H.; Pang, C.; Son, S.; Kim, J. H.; Jang, Y. H.; Kim, D. E.; et al. Conductive Fiber-Based Ultrasensitive Textile Pressure Sensor for Wearable Electronics. *Adv. Mater.* **2015**, *27*, 2433−2439.

(4) Lipomi, D. J.; Vosgueritchian, M.; Tee, B. C.-K.; Hellstrom, S. L.; Lee, J. A.; Fox, C. H.; Bao, Z. Skin-like Pressure and Strain Sensors Based on Transparent Elastic Films of Carbon Nanotubes. *Nat. Nanotechnol.* **2011**, *6*, 788−792.

(5) Fan, F.-R.; Lin, L.; Zhu, G.; Wu, W.; Zhang, R.; Wang, Z. L. Transparent Triboelectric Nanogenerators and Self-Powered Pressure Sensors Based on Micropatterned Plastic Films. *Nano Lett.* **2012**, *12*, 3109−3114.

(6) Kwon, D.; Lee, T.-I.; Shim, J.; Ryu, S.; Kim, M. S.; Kim, S.; Kim, T.-S.; Park, I. Highly Sensitive, Flexible, and Wearable Pressure Sensor Based on a Giant Piezocapacitive Effect of Three-Dimensional Microporous Elastomeric Dielectric Layer. *ACS Appl. Mater. Interfaces* **2016**, *8*, 16922−16931.

(7) Yang, Y.; Zhang, H.; Lin, Z.-H.; Zhou, Y. S.; Jing, Q.; Su, Y.; Yang, J.; Chen, J.; Hu, C.; Wang, Z. L. Human Skin Based Triboelectric Nanogenerators for Harvesting Biomechanical Energy and as Self-Powered Active Tactile Sensor System. *ACS Nano* **2013**, *7*, 9213−9222.

(8) Wang, X.; Dong, L.; Zhang, H.; Yu, R.; Pan, C.; Wang, Z. L. Recent Progress in Electronic Skin. *Adv. Sci.* **2015**, *2*, 1500169.

(9) Zang, Y.; Zhang, F.; Di, C.-a.; Zhu, D. Advances of Flexible Pressure Sensors toward Artificial Intelligence and Health Care Applications. *Mater. Horiz.* **2015**, *2*, 140−156.

(10) Chen, L. Y.; Tee, B. C.-K.; Chortos, A. L.; Schwartz, G.; Tse, V.; Lipomi, D. J.; Wong, H.-S. P.; McConnell, M. V.; Bao, Z. Continuous Wireless Pressure Monitoring and Mapping with Ultra-Small Passive Sensors for Health Monitoring and Critical Care. *Nat. Commun.* **2014**, *5*, 5028.

(11) Mannsfeld, S. C. B.; Tee, B. C.-K.; Stoltenberg, R. M.; Chen, C. V. H.-H.; Barman, S.; Muir, B. V. O.; Sokolov, A. N.; Reese, C.; Bao, Z. Highly Sensitive Flexible Pressure Sensors with Microstructured Rubber Dielectric Layers. *Nat. Mater.* **2010**, *9*, 859−864.

(12) Lee, B.-Y.; Kim, J.; Kim, H.; Kim, C.; Lee, S.-D. Low-Cost Flexible Pressure Sensor Based on Dielectric Elastomer Film with Micro-Pores. *Sens. Actuators, A* **2016**, *240*, 103−109.

(13) Lee, H.; Kwon, D.; Cho, H.; Park, I.; Kim, J. Soft Nanocomposite Based Multi-Point, Multi-Directional Strain Mapping Sensor Using Anisotropic Electrical Impedance Tomography. *Sci. Rep.* **2017**, *7*, 39837.

(14) Majidi, C.; Kramer, R.; Wood, R. J. A Non-Differential Elastomer Curvature Sensor for Softer-than-Skin Electronics. *Smart Mater. Struct.* **2011**, *20*, 105017.

(15) Kim, K.-H.; Hong, S. K.; Jang, N.-S.; Ha, S.-H.; Lee, H. W.; Kim, J.-M. Wearable Resistive Pressure Sensor Based on Highly Flexible Carbon Composite Conductors with Irregular Surface Morphology. *ACS Appl. Mater. Interfaces* **2017**, *9*, 17499−17507.

(16) Tian, H.; Shu, Y.; Wang, X.-F.; Mohammad, M. A.; Bie, Z.; Xie, Q.-Y.; Li, C.; Mi, W.-T.; Yang, Y.; Ren, T.-L. A Graphene-Based Resistive Pressure Sensor with Record-High Sensitivity in a Wide Pressure Range. *Sci. Rep.* **2015**, *5*, 8603.

(17) Cho, S. H.; Lee, S. W.; Yu, S.; Kim, H.; Chang, S.; Kang, D.; Hwang, I.; Kang, H. S.; Jeong, B.; Kim, E. H.; et al. Micropatterned Pyramidal Ionic Gels for Sensing Broad-Range Pressures with High Sensitivity. *ACS Appl. Mater. Interfaces* **2017**, *9*, 10128−10135.

(18) Pan, L.; Chortos, A.; Yu, G.; Wang, Y.; Isaacson, S.; Allen, R.; Shi, Y.; Dauskardt, R.; Bao, Z. An Ultra-Sensitive Resistive Pressure

Sensor Based on Hollow-Sphere Microstructure Induced Elasticity in Conducting Polymer Film. *Nat. Commun.* **2014**, *5*, 3002.
(19) Tee, B. C.-K.; Chortos, A.; Dunn, R. R.; Schwartz, G.; Eason, E.; Bao, Z. Tunable Flexible Pressure Sensors Using Microstructured Elastomer Geometries for Intuitive Electronics. *Adv. Funct. Mater.* **2014**, *24*, 5427−5434.
(20) Kotoh, K.; Nakamuta, M.; Morizono, S.; Kohjima, M.; Arimura, E.; Fukushima, M.; Enjoji, M.; Sakai, H.; Nawata, H. A Multi-Step, Incremental Expansion Method for Radio Frequency Ablation: Optimization of the Procedure to Prevent Increases in Intra-Tumor Pressure and to Reduce the Ablation Time. *Liver Int.* **2005**, *25*, 542−547.
(21) Timsit, R. S. Electrical Contact Resistance: Properties of Stationary Interfaces. *IEEE Trans. Compon. Packag. Technol.* **1999**, *22*, 85−98.
(22) Maseeh, F.; Senturia, S. D. Viscoelasticity and Creep Recovery of Polyimide Thin Films. *IEEE 4th Technical Digest on Solid-State Sensor and Actuator Workshop*; IEEE, 1990; pp 55−60.
(23) Zhang, S.; Mori, S.; Sakane, M.; Nagasawa, T.; Kobayashi, K. Tensile Properties and Viscoelastic Model of a Polyimide Film. *J. Solid Mech. Mater. Eng.* **2012**, *6*, 668−677.
(24) Gong, S.; Zhu, Z. H.; Li, Z. Electron Tunnelling and Hopping Effects on the Temperature Coefficient of Resistance of Carbon Nanotube/Polymer Nanocomposites. *Phys. Chem. Chem. Phys.* **2017**, *19*, 5113−5120.
(25) Cabán-Acevedo, M.; Liang, D.; Chew, K. S.; Degrave, J. P.; Kaiser, N. S.; Jin, S. Synthesis, Characterization, and Variable Range Hopping Transport of Pyrite (FeS2) Nanorods, Nanobelts, and Nanoplates. *ACS Nano* **2013**, *7*, 1731−1739.
(26) Wang, Y.; Pfattner, R.; Jin, L.; Chen, S.; Molina-Lopez, F.; Lissel, F.; Liu, J.; Rabiah, N. I.; Chen, Z.; Chung, J. W.; et al. A Highly Stretchable, Transparent, and Conductive Polymer. *Sci. Adv.* **2017**, *3*, No. e1602076.
(27) El Hasnaoui, M.; Kreit, L.; Costa, L. C.; Achour, M. E. Investigations of Temperature Effect on the Conduction Mechanism of Electrical Conductivity of Copolymer/Carbon Black Composite. *Appl. Microsc.* **2017**, *47*, 121−125.
(28) Kwak, H.-W.; Park, J.-W.; Nam, B.-H.; Yu, A.; Woo, S. M.; Kim, T. H.; Kim, S. H.; Koh, Y. H.; Kim, H. B.; Park, S. J.; et al. Clinical Outcomes of a Cohort Series of Patients with Hepatocellular Carcinoma in a Hepatitis B Virus-Endemic Area. *J. Gastroenterol. Hepatol.* **2014**, *29*, 820−829.
(29) Yang, W.; Yan, K.; Goldberg, S. N.; Ahmed, M.; Lee, J.-C.; Wu, W.; Zhang, Z.-Y.; Wang, S.; Chen, M.-H. Ten-Year Survival of Hepatocellular Carcinoma Patients Undergoing Radiofrequency Ablation as a First-Line Treatment. *World J. Gastroenterol.* **2016**, *22*, 2993−3005.
(30) Sucandy, I.; Cheek, S.; Golas, B. J.; Tsung, A.; Geller, D. A.; Marsh, J. W. Longterm Survival Outcomes of Patients Undergoing Treatment with Radiofrequency Ablation for Hepatocellular Carcinoma and Metastatic Colorectal Cancer Liver Tumors. *HPB* **2016**, *18*, 756−763.
(31) Seo, J. W. Current Status and Future of Radiofrequency Ablation for Hepatocellular Carcinoma. *J. Korean Med. Assoc.* **2015**, *58*, 542−547.
(32) Iida, H.; Aihara, T.; Ikuta, S.; Yamanaka, N. Effectiveness of Impedance Monitoring during Radiofrequency Ablation for Predicting Popping. *World J. Gastroenterol.* **2012**, *18*, 5870−5878.
(33) Livraghi, T.; Goldberg, S. N.; Lazzaroni, S.; Meloni, F.; Solbiati, L.; Gazelle, G. S. Small Hepatocellular Carcinoma: Treatment with Radio-Frequency Ablation versus Ethanol Injection. *Radiology* **1999**, *210*, 655−661.
(34) Kang, T. W.; Lim, H. K.; Lee, M. W.; Kim, Y.-s.; Rhim, H.; Lee, W. J.; Gwak, G.-Y.; Paik, Y. H.; Lim, H. Y.; Kim, M. J. Aggressive Intrasegmental Recurrence of Hepatocellular Carcinoma after Radiofrequency Ablation: Risk Factors and Clinical Significance. *Radiology* **2015**, *276*, 274−285.
(35) del Valle, J.; de la Oliva, N.; Müller, M.; Stieglitz, T.; Navarro, X. Biocompatibility Evaluation of Parylene C and Polyimide as Substrates for Peripheral Nerve Interfaces. *7th International IEEE/EMBS Conference on Neural Engineering (NER) 2015*, July 2015, pp 442−445.
(36) Popov, A. M.; Lozovik, Y. E.; Fiorito, S.; Yahia, L. Biocompatibility and Applications of Carbon Nanotubes in Medical Nanorobots. *Int. J. Nanomed.* **2007**, *2*, 361−372.
(37) Garibaldi, S.; Brunelli, C.; Bavastrello, V.; Ghigliotti, G.; Nicolini, C. Carbon Nanotube Biocompatibility with Cardiac Muscle Cells. *Nanotechnology* **2006**, *17*, 391−397.
(38) Nayagam, D. A. X.; Williams, R. A.; Chen, J.; Magee, K. A.; Irwin, J.; Tan, J.; Innis, P.; Leung, R. T.; Finch, S.; Williams, C. E.; et al. Biocompatibility of Immobilized Aligned Carbon Nanotubes. *Small* **2011**, *7*, 1035−1042.
(39) Seo, J.-M.; Kim, S. J.; Chung, H.; Kim, E. T.; Yu, H. G.; Yu, Y. S. Biocompatibility of Polyimide Microelectrode Array for Retinal Stimulation. *Mater. Sci. Eng., C* **2004**, *24*, 185−189.
(40) Bhatt, V. D.; Teymouri, S.; Melzer, K.; Abdellah, A.; Guttenberg, Z.; Lugli, P. Biocompatibility Tests on Spray Coated Carbon Nanotube and PEDOT:PSS Thin Films. *IEEE Trans. Nanotechnol.* **2016**, *15*, 373−379.
(41) Stauffer, P. R.; Rossetto, F.; Prakash, M.; Neuman, D. G.; Lee, T. Phantom and Animal Tissues for Modelling the Electrical Properties of Human Liver. *Int. J. Hyperther.* **2003**, *19*, 89−101.

https://dx.doi.org/10.1021/acssensors.9b02260
ACS Sens. 2020, 5, 481−489